Sizing the largest ocean waves using the SWOT mission

Fabrice Ardhuin[1]*, Taina Postec[1], Mickael Accensi[1], Jean-François Piolle[1], Guillaume Dodet[1], Marcello Passaro[2], Marine De Carlo[3], Romain Husson[3], Gilles Guitton[4] , Fabrice Collard[4]

Affiliations:

[1]Laboratoire d'Océanographie Physique et Spatiale (LOPS), Univ. Brest, CNRS, IRD, Ifremer, IUEM, Brest, 29200, France.
[2]Deutsches Geodätisches Forschungsinstitut der Technischen Universität München (DGFI-TUM), Munich, Germany.
[3]Division Radar, CLS, Plouzané, 29200, France.
[4]OceanDataLab, Locmaria‑Plouzane, 29200, France.

*Corresponding author. Email: fabrice.ardhuin@univ-brest.fr

Abstract: Extreme storms generate ocean waves, with significant heights that may exceed 20 m. Possible climate trends for these events are unknown as they only cover small ocean areas, often missed by nadir-looking satellite altimeters. Because storm waves radiate as swell across ocean basins, they are resolved by the Surface Water and Ocean Topography (SWOT) satellite mission. We find a very sharp decay of swell heights as a function of distance from the storm, which we link to the low frequency shape of the wave spectrum in the storm, quantified by a storm peak period. This period is a useful metric for sizing storms and their associated swells. With this data, SWOT illuminates the investigation of air-sea interactions, coastal impacts and the interpretation of seismic data.

Given the right conditions, wind-generated waves can grow to extreme sizes, affecting all activities at sea and on the coast. In the context of climate change and a necessary adaptation of oceanic and coastal infrastructure, we need to know the properties of rare events for the assessment of safety conditions of existing structures and the design of new platforms, jetties, wind farms, etc.

Knowledge of the wave climate heavily relies on numerical models that use semi-empirical parameterizations extrapolated to extreme conditions. The most common parameter to describe the wave field is the significant wave height H_s, defined as 4 times the standard deviation of the surface elevation over a 20 minute *in situ* record, or over a few kilometers squared when measured from space (*1*). The distribution of wave energy across frequencies, represented by the frequency spectrum $E(f)$, provides additional important information. The peak frequency f_p for which $E(f)$ maximum, is often used to characterize the dominant waves, and corresponds to the peak period $T_p=1/f_p$.

Observations of ocean waves show that both H_s and T_p grow as the wave field develops, with a tight correlation between both variables (*2,* Fig. S1). Spectra from floating buoys in growing wave conditions follows a shape characterized by a "tail" for frequencies above $2\,f_p$ decaying like the frequency to a power -4 to -5 (*3,* Fig. S2) and a very steep "head" for $f<f_p$. Energy at this head was explained by Hasselmann (*4*,*5*): non-linear wave-wave interactions transfer energy to lower frequencies, making it possible for waves phase speeds, $g/(2\pi f)$ with g the acceleration of gravity, to exceed the wind speed. Detailed calculations of wave-wave interactions suggest that

the wave spectrum is very steep at low frequencies, proportional to f^{-7} (*6*,*7*). It is unknown how much wave-wave interaction theory applies in extreme conditions. The high wind speeds that often come with high waves may introduce additional effects that probably modify wind-wave interactions and wave breaking (*8*), and the investigation of waves in these extreme storms is an important research topic.

Swell dispersion and storm fingerprints

In situ and satellite wave measurements are rare for wave heights over 16 m. This is illustrated here for storm Bolaven, a tropical cyclone that became a very intense extratropical storm in October 2023.

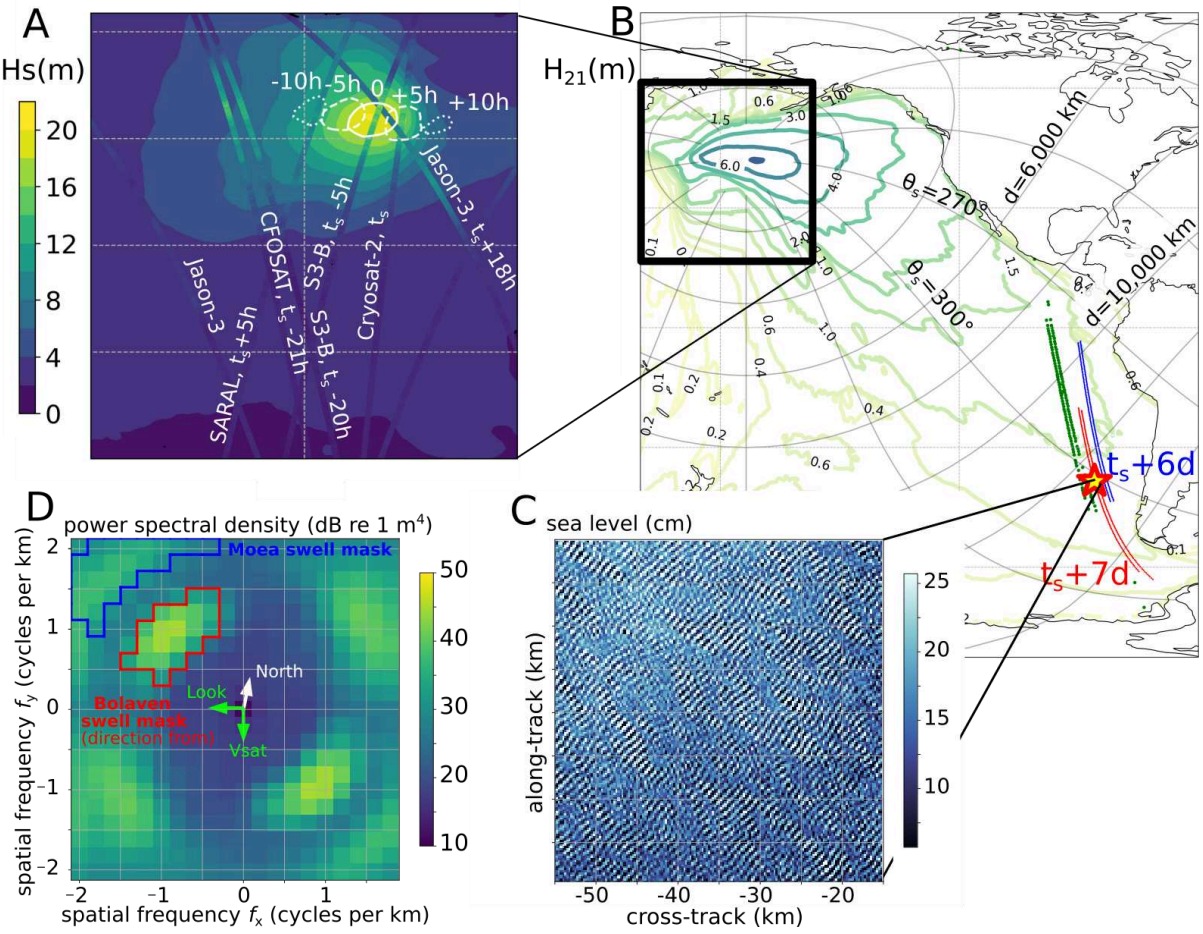

Fig. 1. Example storm and swell field. (**A**) map of modeled wave heights at the time t_s of the storm peak (16 October 1:00 UTC), and altimeter measurements within 20 hours (t_s-20 to t_s+20h) from Jason-3, Cryosat-2, SARAL, CFOSAT, Sentinel-3B (**B**) contours of the maximum modeled value of H_{21} from October 15 to 27, label units are meters, and a subset of locations of SWOT measurements where Bolaven swells are observed, including blue dots for track 300 on 23 October, red dots for track 328 on 24 October. Green dots are locations of CFOSAT swell data on 23 October. At the location of the red star, 38.1°S 274.6°E, (**C**) is an example SWOT surface elevation field, and (**D**) the corresponding wave spectrum. The region inside the red and blue polygons corresponds to our masks for swells from storms Bolaven and Moea.

According to a wave model (*9*) the significant wave height reached 20.3 m, the largest value globally for the entire year 2023. The modeled H_s exceeds 18 m in a region smaller than 300 km (white contours in Fig. 1A) that appears on October 15 at 12 h UTC, moves rapidly to the east and vanishes 24 hours later. No satellite track comes closer than 300 km of the maximum modeled value. The maximum H_s estimated from the Sentinel-3B satellite altimeter is only 15.4±0.2m, when sampling-induced fluctuations are properly filtered (*1*). Are the modeled values above 20 m a numerical hallucination, or is the model underestimating even larger true wave heights, as it has been often reported (*10*)?

Observing swells away from the storm provides a different point of view, and a much larger region of interest. In numerical models we can compute a partial wave height H_{21} from the wave energy for periods longer than 21 s. Figure 1B shows how these long waves start from a short-lived and compact energy pulse, then expands over 2 weeks, dispersing across half of the Pacific (Movie S1). Separating these long swells from other waves requires measurements that resolve the wavelength of these swells.

This investigation is made possible by maps of the sea surface elevation provided by the SWOT satellite mission at 250 m resolution (*11,12*, Fig. 1C). SWOT measurements cover two 50-km wide swaths on both sides, left and right, of the satellite track. These data resolve swells with wavelengths longer than about 500 m, which corresponds to a deep-water linear wave period of 18 s (*13*). The Fourier transform of the surface elevation produces swell spectra $E(f_x,f_y)$ with f_x and f_y the spatial frequencies in the satellite cross-track and along-track directions (*14*, Fig. 1D). SWOT spectra typically contain a few energetic peaks that correspond to swells easily associated with well-defined storm events (*15*). With a very low instrument noise level, SWOT is able to measure swell heights as low as 3 cm (*13*). These unique capabilities allow measurements of swell "fore-runners", those components with frequencies below the peak frequency in the storm, that propagate on the leading edge of the swell field (*16*).

Previous studies of swells focused on the dominant periods and their interactions with topography, currents, or the atmosphere. Theory predicts a constant spectral density when decomposed in frequency and direction (*17*). Pioneering work using pressure time series recorded at near-shore locations located across the Pacific are consistent with the theory, with very weak dissipation for periods longer than 15 s (*18*). Satellite-based synthetic aperture radars provided more accurate estimates of the dissipation of dominant swells across ocean basins (*19*,*20*).

Here we focus on the longest possible swells, and quantify storm intensity from their properties. We use the "energy wavelength" L_E and investigate how the swell height H_{ss} (*15*) varies as a function of distance d from the storm, along a great circle. For propagation paths away from islands, all storms exhibit the same pattern. The wavelength increases like d^2 (Fig. 2A), as expected from the dispersion of linear waves (*16*). From a compact source on October 16 (Fig. 1A), the wave field expands to cover half of the Pacific over a week later (Fig. 1B). A more puzzling feature, previously unreported, is the sharp decrease in swell height, with a power law d^{-n} with $n \approx 9$ (Fig. 2B).

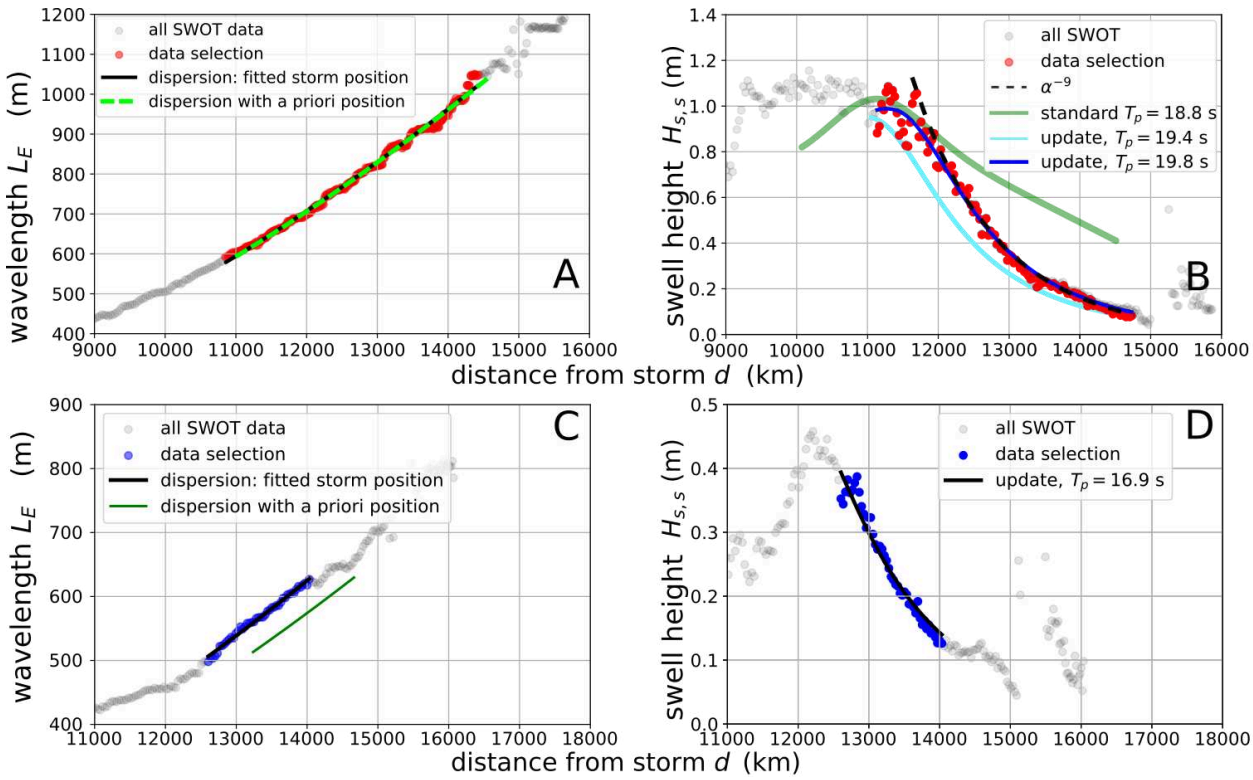

Fig. 2. Wavelength and height of swell from storm Bolaven for SWOT cycle 005 track 328 (red dots in Fig. 1.B), and storm Moea (SWOT cycle 005 track 300, blue dots in Fig. 1.B). (**A**) The increase in wavelength is consistent with dispersion from a compact source, which we use to refine the storm position and time. (**B**) The observed decay in swell height can be explained by wave propagation assuming a shape of the wave spectrum in the storm. The standard spectral shapes (*5*) is updated (*15*) to estimate a storm peak period T_p. The fitted values are weakly sensitive to the data selected for the fit (red dots), and a 2% lower T_p (light blue line) is clearly not compatible with the SWOT measurements. For the weaker storm Moea (**C**), waves have shorter wavelengths and (**D**) lower wave heights.

Swell energy, proportional to the square of the swell height, thus decay like d^{-18}. This energy is a spectral density multiplied by the spectral width in frequency that, in theory, varies like $1/d$, and the width in direction that, neglecting the effect of currents, varies like $1/\sin(d/R_E)$ with R_E the Earth radius (*13*). Neglecting energy dissipation, spectral densities are conserved along the propagation path (*10*). As a result, for any azimuth, for example θ_s =300° in Fig. 1B, the wave spectrum in the storm $E(f,\theta_s)$ should vary like f^{17}.

This steep spectrum slope is consistent with the idea that wave-wave interaction theory explains most of the energy below the spectral peak (*5*), but it is not consistent with standard empirical shapes (*5*). Those spectral shapes are poorly constrained by data for $f < f_p$, because very high spectral resolution is needed to resolve this sharp variation. Numerical simulations of the inverse energy cascade associated with wave-wave interactions give exponents 16–17 for $0.5\,f_p < f < 0.9\,f_p$ (*6,7*). We thus propose an update of the standard spectral shape in the range $f < f_p$, including a f^{17} slope and a smooth adjustment around the peak (*15,* Fig. S2). This updated spectrum gives a much better fit to the observations (Fig. 1B,D), and this fit provides a means to estimate $T_p = 1/f_p$ in the storm, a parameter that we will call "storm peak period (SPP)" to avoid confusion with the local swell peak period.

Fitting a wider range of wavelengths generally produces slightly lower peak periods, possibly because of a combination of lower periods over a larger area around the storm center (*15,* Fig. S4). We have thus performed a 2-step fit to keep the largest wavelengths (*15*) and this analysis was repeated for different satellite tracks (Table S2). Combining all tracks, the estimated value, T_p=19.3±0.4 s, is close to the modeled value at the peak of the storm T_p=19.6 s. Using Toba's empirical relationship (*2*) between T_p and H_s, together with a modeled wind of 30 m/s (*21*) and a drag coefficient of 0.0025, leads to a value $H_s \simeq$19 m. Alternatively, we may use the measured energy level of the swell. From the data in Fig. 2.B, the spatial integration of the Bolaven swell energy is 4.5 PJ per radian for $\theta_s \cong 300°$ and waves longer than 575 m. Where available, combining measurements from all θ_s directions gives a total radiated energy, and its estimation at different times would give a swell dissipation rate.

This analysis provides estimations of storm peak period (SPP) for the largest storms but it does not apply to storms for which the dominant waves are not resolved. For storm Moea (Fig. 2C,D) keeping all the data with L_E > 500 m gives a first step fit T_p=16.9 s (Fig. 2D) but this can be an artifact of the missing energy of shorter waves not resolved by SWOT. Moea swells have a power density of 0.09 PJ per radian for waves longer than 575 m. This value is 50 times lower than the 4.5 PJ of Bolaven, and illustrates the very rapid decrease in low frequency energy as the storm peak period decreases.

Building a storm catalog

Several databases exist for storm tracks (*21,22*) and in particular tropical storms (*23*), but no database has used tracks based on wave properties, including their low frequency content. This prevents some easy identification of low frequency signals in buoy data or in seismic measurements (*25*). Moreover, a long-term storm wave database would help the determination of possible climate trends currently suggested by CMIP-6-forced wave model ensemble analysis (*26*, *27*)

We started our catalog from two complementary storm track databases, one obtained by following the maxima of H_s in the LOPS-CCI model hindcast (*28*) and the second obtained by finding maxima in H_s measurements from denoised and inter-calibrated satellite altimeter data (*29*), which is available up to December 2023. For the year 2023 this includes SARAL, Jason-3, Sentinel-3A, Sentinel-3B, Sentinel-6, Cryosat-2. To simplify the discussion, we gave names to storms that appeared to not have a name yet (Fig. 3, Table 1 and Table S1). For the year 2023 and 2024 we added data from two other altimeters: the nadir beam of the Surface Wave Investigation and Monitoring (SWIM) instrument on board the China-France Ocean Satellite (CFOSAT) and Poseidon-3C which is the nadir altimeter on board SWOT. We combine both databases to produce a merged storm catalog (*30*), now including peak periods estimated from SWOT from March 2023 to December 2024 (Fig. 3).

The locations of the most severe storms for 2023 and 2024 follow the usual storm tracks with the most intense storms in the North Pacific and North Atlantic. Kirk and Bolaven are tropical storms that re-intensified as extra-tropical storms. We have searched for satellite maxima within 1,000 km and 24 hours of the model maxima. Fig. 3B confirms that altimeters generally miss the peak of the storms and give maximum altimeter wave heights (MAWH) that are on average 2.2 m lower than the modeled maximum value (MMWH). MAWH and MMWH are poorly correlated (r=0.59) and the MAWH is a lower bound on the storm maximum wave height but a poor discriminator of storm intensity.

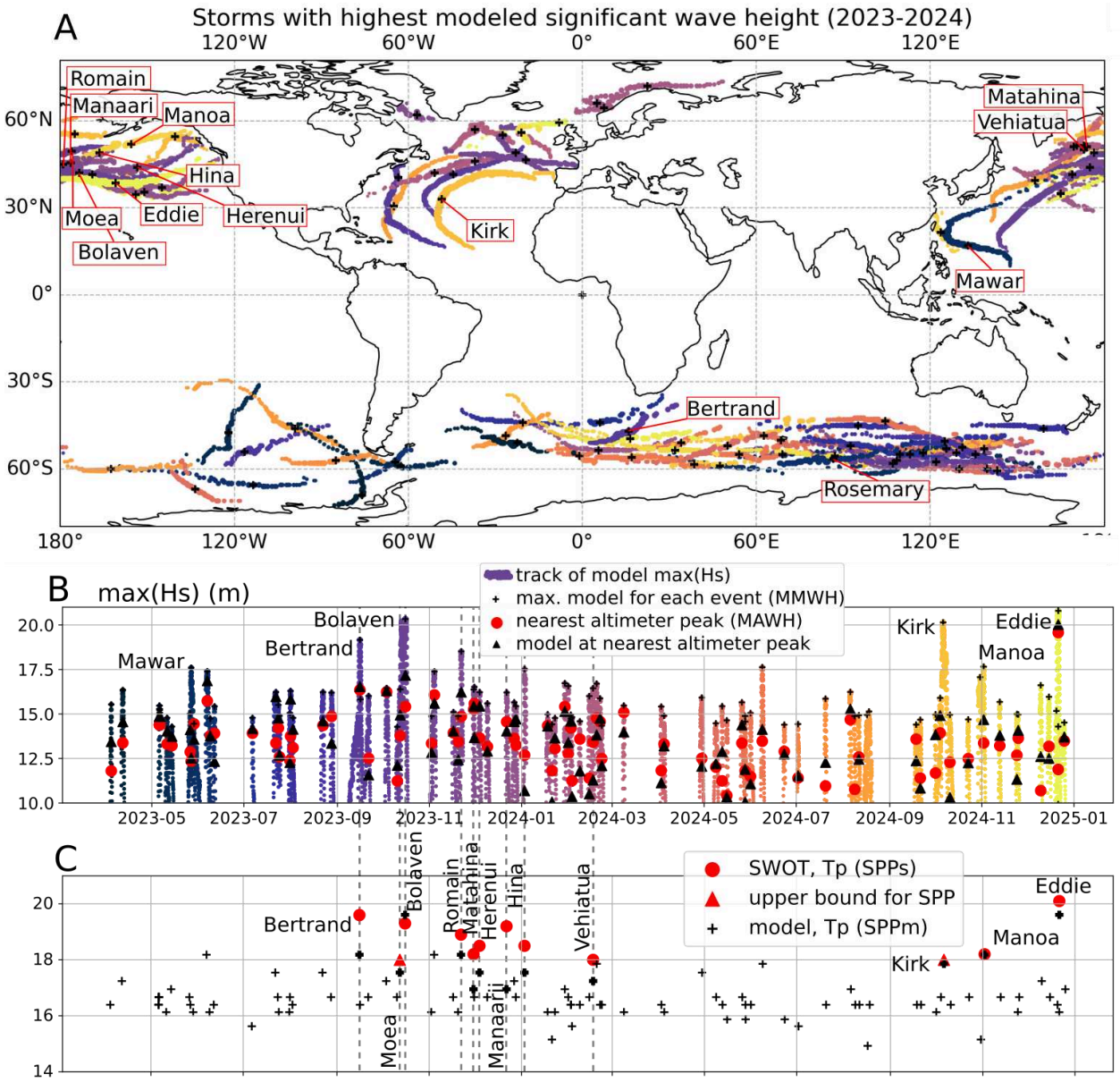

Fig. 3. Storm catalog combining model, nadir altimeters – 8 satellites in 2023 and 2 in 2024 – and SWOT data. (**A**) map of the 100 most severe storms from April 2023 to December 2024, with the tracks of the most severe storms plotted on top of the weaker ones. Storm tracks are provided by a numerical model (*9*) and colored by time. (**B**) time series of modeled H_s along the tracks (same colors as in A), and corresponding highest altimeter H_s (**C**) storm peak periods (SPP) at the location of the storm H_s maximum.

The fact that the model at the same location as the altimeter (MSLA) is highly correlated with the satellite value at the same location (r=0.98, bias =0.3 m, root mean square difference =0.95 m) is an important statistical validation of the model for extremes, but it does not say much about possible model errors in any particular event.

Storm peak periods estimated from SWOT provide a complementary measure of the storm intensity. We named the most intense event “Eddie”. This is an extratropical storm that allowed the big wave surfing competition “the Eddie” in Hawaii, and caused casualties and extensive damage on the American coasts from Canada to Peru. That information is generally

consistent with model estimates for storm peak periods over 18 s (Fig. 3C). For some storms (Moea and Kirk) we could not identify a maximum swell height and we concluded that the SWOT resolution limit at 18 s must be an upper bound for the SPP. Combined with our analytical swell propagation model (Fig. 2), SPPs can be used to estimate the possible magnitude of very long period swells radiated by these storms.

SWOT data contains long swells from all of the most severe storms that occurred after March 2023, and we have focused our analysis on North Pacific storms that are easier to interpret as they propagate away from islands. We only analyzed 10 storms and the relation between MMWH and SPPs estimated from SWOT is not simple. We find that Eddie had both the longest periods and highest waves (Fig. S5, Table 1), and Kirk's low period is consistent with Toba's law, with shorter periods for higher wind speeds (*2*). Wind speeds do not explain everything, and further analysis of the storm translation speed and azimuth relative to the dominant wave direction will be needed to understand SPP differences under 1 s, such as the higher value for storm Manaarii. Ocean currents may also have some influence, and the larger SPP value for Bertrand, compared to the model output, could be related to a model underestimation of wave-current interactions in the Agulhas region.

We have also tested our analysis method with the 10° incidence off-nadir beam on CFOSAT/SWIM. CFOSAT was launched in 2018 and resolves waves down to 50 m wavelength, using a real aperture radar (*31*). We processed Level 2S data produced by Ifremer (*32*), which gives swell height, wavelength and direction. Fig. 4 shows the SWIM data and selection for the satellite track shown in Fig. 1B, together with the nearest SWOT data (observed 9 hours later). For wavelengths above 800 m, SWIM is able to detect swells with heights above 0.2 m. The swell heights from SWIM have a larger scatter than the SWOT data, probably due to fluctuations in the modulation of short waves by long waves that define the SWIM radar measurement from which swell heights are estimated (*32*).

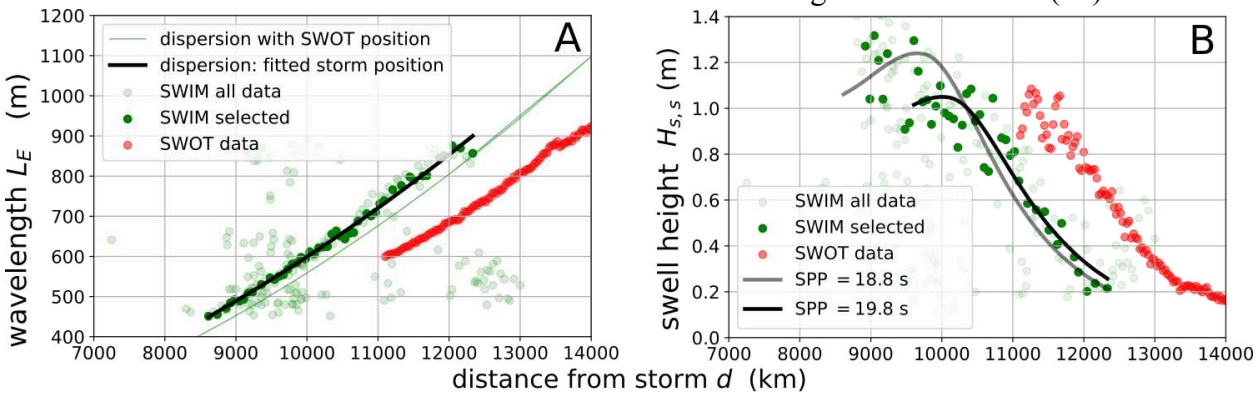

Fig. 4. Estimation of storm peak period using SWIM 10° beam data, acquired along the green track of Fig. 1.B, 9 hours before the SWOT data along the red track. (A) wavelength and (B) swell heights and fitted swell height (grey and black curves) using either all good data or only data with $L_E > 550$ m.

In this preliminary test for storm Bolaven, we obtained SPP values that ranged from 18.8 to 19.8 s depending on the selection criteria of the data. Using an uncertainty model for the SWIM swell heights, one might obtain useful storm peak periods estimates, allowing an extension of our catalog back to 2019.

Before 2019, our knowledge of past storms can further benefit from SWOT swell properties measured near seismic stations that have operated for over a century (*33*), providing a

calibration of the transfer function from microseism amplitudes to wave heights. This could help reconciliate diverging trends in microseism and ocean wave energy (*34*,*35*). Looking further back in time, our SWOT estimates of peak periods associated with extreme wave heights will also help reinterpret paleostorm data (*36*).

Recent storms in perspective

The SWOT era has just started and the data reported here cover less than 2 years. SWOT provides information on storm properties that is complementary to existing data from models, buoys and nadir altimeters (*37*). When sorted by modeled maximum wave height SWOT has observed 8 of the top 250 storms of the past 34 years (Table 1), and we could quantify the storm peak period for 5 of these.

rank	date	lon.(°)	lat.(°)	wind speed	wave dir.	Hs (m) (MMWH)	model Tp (s)	SWOT SPP (s)	Hs sat. (MAWH)	Hs mod. (MSLA)	storm name
	at the time and location of the model max. Hs								at sat. max. Hs		
1	20140105	031W	47N	31.8	258	23.0	20.4		18.7±0.2	18.4	Ronadh*
2	20130115	166E	39N	29.9	346	22.2	20.0		15.8±0.2	16.8	Paul*
3	19981026	177W	412N	32.1	249	21.6	20.0		12.6±0.2	15.4	Yoshiaki*
4	20150427	138E	56S	28.9	239	21.0	20.0		18.1±0.3	19.6	Luigi*
5	20241221	161E	39N	28.9	273	20.8	19.6	20.1±0.5	19.7±0.3	20.2	Eddie*
6	20100925	155W	42N	31.3	222	20.7	19.6		15.0±0.2	17.7	Malakas
7	20081022	172W	49N	32.0	254	20.7	19.2		11.2±0.1	11.7	Nobuhito*
8	20210130	45W	42N	29.0	231	20.6	18.9		18.3±0.3	18.2	Laurent*
9	20220208	26W	64N	33.7	216	20.5	18.9		18.9±0.2	15.8	Danièle*
10	20060902	158E	24N	43.5	83	20.4	17.9		14.1±0.1	17.7	Ioke
11	20060203	171E	44N	30.8	259	20.4	19.6		18.0±0.2	15.8	Helen*
12	20231016	174W	42N	30.0	264	20.3	19.6	19.3±0.4	15.4±0.2	17.2	Bolaven
17	20241006	49W	33N	39.4	175	20.1	17.9	< 18	-	-	Kirk
56	20230915	16E	47S	30.6	244	19.2	18.2	19.6±0.5	16.4±0.2	16.5	Bertrand*
92	20231122	179W	45N	29.2	267	18.5	18.2	18.9±0.3	15.0±0.2	16.1	Romain*
192	20241102	156W	52N	27.4	252	17.7	18.2	18.2±0.1	13.4±0.2	14.7	Manoa*
206	20230527	133E	17N	43.1	77	17.6	16.4	-	12.7±0.1	12.5	Mawar
234	20230606	87E	57S	26.2	254	17.4	18.2	-	15.7±0.2	16.8	Rosemary
489	20231012	176W	50N	26.4	255	16.4	17.5	< 18	13.7±0.2	14.9	Moea*

Table 1. Properties of the top storms (ranked by modeled maximum significant wave height), for the years 1991-2024, and 2023-2024 (shaded in blue). Wave direction is the mean wave direction from where the waves propagate. Storm names with an asterisk are preliminary and were given by the authors.

Many of these storms were unnamed, and only two in the top 20 (Ioke and Kirk) were active tropical storms at the time of the modeled maximum H_s. Tropical storms had the highest wind speeds (44 m/s for Ioke), but a relatively lower peak period for its wave height, consistent with Toba's empirical law that relates wave heights and periods (Fig. S2). Swell

observations by SWOT are unique in providing observations that confirm Toba's law and wave evolution physics for the largest wave heights, providing a much needed verification of numerical wave models. Storms are not uniquely defined by wave heights, and the associated periods are key variables for most applications including the estimation of air-sea fluxes (*38*), or coastal impacts (*39*).

Conclusions

Measurements of wave heights from traditional satellite altimetry have provided a sparse sampling of the ocean wave field since 1991, poorly capturing extreme events. Using the unique capability of SWOT to measure long swells, we have obtained SWOT measurements for all of the largest storms, those with a significant wave height that reached at least 16 m. There are 20 such events every year on average, and many weaker storms are also detected. Each swell field contains fingerprints of its generating storm. We estimated wave periods in the storms from the swell heights at the leading edge of the swell fields, 5,000 to 20,000 km away: the most severe storm had a peak period of 20.1±0.5 s, consistent with measured wave heights of 19.7±0.3 m in the storm. At a distance of 5000 km, we found swells higher than 0.2 m with a mean wavelength exceeding 1,200 m, which corresponds to a period of 28 s. SWOT data suggest that the standard parametric spectral shapes (*5*), used in all engineering applications, should be revised as they overestimate low frequency energy. This updated spectral shape and our parametric swell model (*15*) will certainly be useful in a wide range of engineering and geophysical applications for which wave periods are essential parameters. These include the interpretation of sedimentary records (*36*) and the analysis of yet unexplained seismic signals at periods 18 to 26 s, possibly associated with ocean waves (*25*). In turn, SWOT can be used to calibrate seismic observations (*34*). Such a calibrated climate record is needed to reduce the uncertainty in the variability and trends for wave extremes that are generally estimated from models in a range of conditions for which they were not designed and for which they have not yet been validated. These are critically important for adaptation to climate change, in particular in coastal areas.

References and Notes

1. M. De Carlo, F. Ardhuin, Along-track resolution and uncertainty of altimeter-derived wave height and sea level: re-defining the significant wave height in extreme storms. *J. Geophys. Res. Oceans* **134**, (2024). doi: 10.1029/2023JC020832
2. Y. Toba, Local balance in the air-sea boundary processes. III On the spectrum of wind waves, *J. Oceanogr. Soc. Japan* **29**, 209–220 (1973). doi: 10.1007/BF02109506
3. L. Lenain, W. K. Melville, Measurements of the directional spectrum across the equilibrium saturation ranges of wind-generated surface waves, *J. Phys. Oceanogr.* **47**, 2123–2138 (2017). doi: 10.1175/jpo-d-17-0017.1
4. K. Hasselmann, On the non-linear energy transfer in a gravity wave spectrum, part 1: general theory, *J. Fluid Mech.* **12**, 481–501 (1962). doi: 10.1017/S0022112062000373
5. K. Hasselmann and T. P. Barnett and E. Bouws and H. Carlson and D. E. Cartwright and K. Enke and J. A. Ewing and H. Gienapp and D. E. Hasselmann and P. Kruseman and A. Meerburg and P. Müller and D. J. Olbers and K. Richter and W. Sell and H. Walden,

Measurements of wind-wave growth and swell decay during the Joint North Sea Wave Project, *Deut. Hydrogr. Zeit.* **8**, 1–95 (1973).

6. I. V. Lavrenov, A Numerical Study of a Nonstationary Solution of the Hasselmann Equation, *J. Phys. Oceanogr.*, **33** (2003). doi: 10.1175/1520-0485(2003)033<0499:ANSOAN>2.0.CO;2
7. S. I. Badulin, V. E. Zakharov, Ocean swell within the kinetic equation for water waves. *Nonlin. Processes Geophys.* **24**, 237–253 (2017). doi:10.5194/npg-24-237-2017
8. A. V. Soloviev, R. Lukas, M. A. Donelan, B. K. Haus, I. Ginis, The air-sea interface and surface stress under tropical cyclones, *Sci. Rep.* **4**, 5306 (2014). doi:10.1038/srep05306
9. M. Accensi (2024). GLOB-30M_LOPS_2025. IFREMER, doi: 10.12770/87209a81-2c27-452b-86ae-b9c2cc4d43a9
10. L. Cavaleri, Wave modelling: missing the peaks, *J. Phys. Oceanogr.* **39**, 2557–2778 (2009). doi: 10.1175/2009JPO4067.1
11. L.-L. Fu, T. Pavelsky, J.-F. Cretaux, R. Morrow, J. T. Farrar, P. Vaze, The Surface Water and Ocean Topography Mission: A Breakthrough in Radar Remote Sensing of the Ocean and Land Surface Water. *Geophys. Res. Lett.* **51**, e2023GL107652 (2024). doi: 10.1029/2023GL107652.
12. SWOT project. (2023). Swot level‐2 Karin low rate SSH unsmoothed, reprocessed version c products (v2.0) [Dataset]. CNES. https://doi.org/10.24400/527896/A01‐2023.016
13. F. Ardhuin, B. Molero, A. Bohé, F. Nouguier, F. Collard, I. Houghton, A. Hay, B. Legresy, Phase-resolved swells across ocean basins in SWOT altimetry data: revealing centimeter-scale wave heights including coastal reflection. *Geophys. Res. Lett.* **51**, e2024GL109658 (2024). doi: 10.1029/2024GL109658
14. The SWOT_L3_LR_WIND_WAVE product, derived from the SWOT_L3_LR_SSH product, is produced and made freely available by AVISO, DUACS and LOPS teams as part of the DESMOS and VAGUES Science Team projects". AVISO/DUACS., 2025. SWOT Level-3 KaRIn Wind Wave (v2.0) [Data set]. CNES. doi:10.24400/527896/a01-2024.016
15. Materials and methods are available as supplementary materials online.
16. W. Munk, Tracking Storms by Forerunners of Swell, *J. Atmos. Sci.* **4**, 45–57 (1947). doi:10.1175/1520-0469(1947)004<0045:TSBFOS>2.0.CO;2)
17. G. W. Groves, Geometric wave propagation through curved media, *J. Geophys. Res.* **71**, 5271–7274 (1966). doi: 10.1029/JZ071i022p05271
18. F. E. Snodgrass, G. W. Groves, K. Hasselmann, G. R. Miller, W. H. Munk, W. H. Powers, Propagation of ocean swell across the Pacific, *Phil. Trans. Roy. Soc.* **A249**, 431–497 (1966).
19. F. Collard, F. Ardhuin, B. Chapron, Monitoring and analysis of ocean swell fields from space: New methods for routine observations. *J. Geophys. Res.* **114**, C07023 (2009). doi: 10.1029/2008JC005215
20. F. Ardhuin, B. Chapron, F. Collard, Observation of swell dissipation across oceans, *Geophys. Res. Lett.* **36**, L06607 (2009). doi: 10.1029/2008GL037030
21. H. Hersbach et al., The ERA5 global reanalysis. *Quart. J. Roy. Met. Soc.* **146**, 1999–2049 (2020). doi:10.1002/qj.3803

22. J. Lodise, S. Merrifield, C. Collins, P. Rogowski, J. Behrens, E. Terrill, Global climatology of extratropical cyclones from a new tracking approach and associated wave heights from satellite radar altimeter. *J. Geophys. Res. Oceans* **127**, e2022JC018925 (2022). doi:10.1029/2022JC01892524

23. Bengtsson, L., K. I. Hodges, E. Roeckner, Storm tracks and climate change, *J. Cli.* **19**, 3518-3543 (2006). doi: 10.1175/JCLI3815.1

24. K. R. Knapp, M. C. Kruk, D. H. Levinson, H. J. Diamond, C. J. Neumann, the international best track archive for climate stewardship (IBTrACS). *Bull. Amer. Met. Soc.* **91**, 363–376 (2010). doi: 10.1175/2009BAMS2755.1

25. C. Bruland, C. Hadziioannou, Gliding tremors associated with the 26 second microseism in the Gulf of Guinea, *Nature Comm. Earth & Env.* **4** (2023). doi: 10.1038/s43247-023-00837-y

26. L. Erikson, J. Morim, M. Hemer, I. Young, X. L. Wang, L. Mentaschi, N. Mori, A. Semedo, J. Stopa, V. Grigorieva, S. Gulev, O. Aarnes, J.-R. Bidlot, Ø. Breivik, L. Bricheno, T. Shimura, M. Menendez, M. Markina, V. Sharmar, C. Trenham, J. Wolf, C. Appendini, S. Caires, N. Groll, A. Webb, Global ocean wave fields show consistent regional trends between 1980 and 2014 in a multi-product ensemble. *Commun. Earth Environ.* **3**, 1–16 (2024). doi:10.1038/s43247-022-00654-9

27. A. Meucci, I. R. Young, M. Hemer, E. Kirezci, R. Ranasinghe, Projected 21st century changes in extreme wind-wave events. *Science Advances* **6**, eaaz7295 (2020). doi:10.1126/sciadv.aaz7295$

28. F. Ardhuin, M. De Carlo, Storm tracks based on wave heights from LOPS WAVEWATCH III hindcast and ERA5 reanalysis, years 1991-2024, SEANOE (2025). doi: 10.17882/105148

29. F. Ardhuin, a database of “very high” and “phenomenal” sea states from the ESA Seastate CCI V4 database, with complements from CNES CFOSAT and SWOT nadir altimeters. Version 1 (not inter-calibrated). SEANOE (2025). doi:10.17882/105378

30. F. Ardhuin, T. Postec, Storm tracks, wave heights and peak periods for “phenomenal” sea states, combining model, altimeter wave heights and swells measured by the SWOT satellite mission. Version 1. SEANOE (2025). doi: 10.17882/105447

31. D. Hauser, C. Tourain, L. Hermozo, D. Alraddawi, L. Aouf, B. Chapron, A. Dalphinet, L. Delaye, M. Dalila, E. Dormy, F. Gouillon, V. Gressani, A. Grouazel, G. Guitton, R. Husson, A. Mironov, A. mouche, A. Ollivier, L. Oruba, F. Piras, R. Rodriguez Suquet, P. Schippers, C. Tison, N. Tran, New Observations From the SWIM Radar On-Board CFOSAT: Instrument Validation and Ocean Wave Measurement Assessment, *IEEE Trans. Geosci. Remote Sens.* (2020): doi: 10.1109/tgrs.2020.2994372

32. Ifremer / CERSAT. 2022. Global Ocean Directional Wave Parameters Level 2S from SWIM onboard CFOSAT for IWWOC project. Ver. 1.0. Ifremer, Plouzane, France. Dataset accessed [2025-03-01]. DOI: 10.12770/12cfed8d-7645-442b-b8ef-a8d08decbaed

33. P. Bernard, Historical sketch of microseisms from past to future, *Phys. Earth Planetary Interiors* **63**, 145–150 (1990). doi:0031-9201(90)90013-N

34. R. Aster, A. T. Ringler, R. E. Anthony, T. A. Lee, Increasing ocean wave energy observed in Earth’s seismic wavefield since the late 20th century, *Nature Communications* **14**, 6984 (2023). doi:10.1038/s41467-023-42673-w

35. M. Casas-Prat, M. A. Hemer, G. Dodet, J. Morim, X. L. Wang, N. Mori, I. Young, L. Erikson, B. Kamranzad, P. Kumar, M. Menéndez, Wind-wave climate changes and their impacts, *Nature Reviews Earth & Environment* **5**, 23-42 (2024).

36. P. A. Allen, P. F. Hoffman, Extreme winds and waves in the aftermath of a Neoproterozoic glaciation, *Nature* **433** (2005) . doi:10.1038/nature03176

37. J. Hanafin, Y. Quilfen, F. Ardhuin, J. Sienkiewicz, P. Queffeulou, M. Obrebski, B. Chapron, N. Reul, F. Collard, D. Corman, E. B. de Azevedo, D. Vandemark, E. Stutzmann, Phenomenal sea states and swell radiation: a comprehensive analysis of the 12-16 February 2011 North Atlantic storms, *Bull. Amer. Met. Soc.* **93**, 1825–1832. doi:10.1175/BAMS-D-11-00128.1.

38. N. Takagaki, S. Komori, N. Suzuki, K. Iwano,T. Kuramoto, S. Shimada, R. Kurose, K. Takahashi, Strong correlation between the drag coefficient and the shape of the wind sea spectrum over a broad range of wind speeds, *Geophys. Res. Lett.* **39**, L23604 (2012). doi:10.1029/2012GL053988

39. G. Dodet, A. Melet, F. Ardhuin X. Bertin D. Idier, R. Almar, The Contribution of Wind-Generated Waves to Coastal Sea-Level Changes, *Surveys in Geophysics* **40**, 1563 (2019). doi:10.1007/s10712-019-09557-5

40. J. L. Hanson, O. M. Phillips, Automated Analysis of Ocean Surface Directional Wave Spectra, *J. Ocean Atmos. Tech.* **18**, 277–293.

41. F. Ardhuin, B. Chapron, F. Collard, Observation of swell dissipation across oceans, *Geophys. Res. Lett.* **36**, L06607 (2009). doi:10.1029/2008GL037030

42. W. J. Pierson, Jr, L. Moskowitz, A proposed spectral form for fully developed wind seas based on the similarity theory of S. A. Kitaigorodskii, *J. Geophys. Res.* **69**, 5,181–5,190 (1964).

43. T. Elfouhaily, B. Chapron, K. Katsaros, D. Vandemark, A unified directional spectrum for long and short wind-driven waves, *J. Geophys. Res.* **102**, 15781–15796 (1997). doi:10.1029/97jc00467

Acknowledgments: We appreciate discussions with Sergey Badulin and Bertrand Chapron on wave-wave interactions and spectral shapes. The SWOT mission is jointly developed by NASA and CNES with contributions from the Canadian Space Agency (CSA) and the United Kingdom Space Agency.

Funding:

European Space Agency grant XXXX (FA, TP, MA, GD, MP)

Centre National d'Etude Spatiales grant YYYY (MdC)

Author contributions: Conceptualization: FA, FC, Methodology: FA, GD, MP, MdC,

Investigation: FA, TP, MA, JFP, GD, MP, Visualization: FA, Funding acquisition: FA, JFP, FC, GD, MP, Supervision: FA, Writing – original draft: FA, Writing – review & editing: FA, GD, MdC, TP, JFP

Competing interests: Authors declare that they have no competing interests.

Data and materials availability: The SWOT L2 ocean data Version C was downloaded from AVISO in January 2025 (*16*), and model output was generated in January 2025 (*9*). Codes generated for data processing and plotting in the paper are available from SEANOE (*27*).

Supplementary Materials

Materials and Methods

Figs. S1 to S5

Tables S1

Movies S1

Science
AAAS

Supplementary Materials for

Sizing the largest ocean waves using the SWOT mission

Fabrice Ardhuin, Taina Postec, Mickael Accensi, Jean-François Piolle, Guillaume Dodet, Marcello Passaro, Marine De Carlo, Romain Husson, Gilles Guitton, Fabrice Collard

Corresponding author: fabrice.ardhuin@univ-brest.fr

The PDF file includes:

Other Supplementary Materials for this manuscript include the following:

Materials and Methods

Defining swell partitions in SWOT spectra, and associated swell heights and wavelengths

Surface elevation spectra were obtained from 40 by 40 km "boxes" (e.g. the location of each blue or red dot in Fig. 1B is the center of one of these boxes). Spectra were computed using 5 by 5 km tiles with a 2-dimensional Hann window, giving a relatively coarse spectral resolution and spectral peaks that are blurred by the Fourier transform of the Hann window: these are minor issues for our analysis in which we only use the energy summed over a large region of the spectrum. The benefit of using relatively small tiles is a large number of degrees of freedom (ndof=128), giving a very low spectral noise. The tiles contain 20 SWOT pixels in the cross-track direction, sampled at 250 m, and 21 pixels in the along-track direction, sampled at 235 m, giving a nearly isotropic spectral resolution of 0.1 cycle per kilometer. This resolution is sufficient for wavelengths up to 1,200 m (see also Fig. S5), with smoothly varying integrated parameters H_{ss} and L_E (defined below).

The spectra include corrections for instrumental effects (*13*) and are double-sided: the energy of waves from one direction is split in two halves that appear at opposite directions. We note that this 180° ambiguity in the propagation direction can be lifted by using the cross-spectra between sea level and radar back-scatter, at least in the case where not all the swell energy propagates perpendicular to the satellite track (*13*). In the present work we rely on the fact that sources of very long waves are associated with a small number of very large storms with time and positions known well enough. Here we use the time and positions of the maximum H_s for storm tracks given by (*27*). In order to isolate the swell contribution for a given storm, we mask the spectrum to only keep spectral components that could reasonably come from a known storm position and time. We first compute the spatial frequencies (f_{xc},f_{yc}) that are consistent with surface gravity from the a priori position and time of the storm peak. We mask the data around that component using the two criteria:

- We keep spectra components that have spatial frequencies within 30% of $k_c=|f_{xc},f_{yc}|$ or that correspond to source locations within 1000 km of the storm peak. The first condition is more restrictive than the second for larger distances from the storm.
- We keep spectral components that have a propagation direction that is with arccos(0.89) from the expected arrival direction.

We have visually inspected the resulting spectra and partition to make sure that the mask boundary (e.g. red line in Fig. 1D) does not cut through a spectral peak: this is why we generally do not use swell fields for which the peak wavelength is less than 550 m, which is often too close to the boundaries of the spectral domain. These storm-based criteria work generally well at large distances (> 7000 km) from the storm center, but they can be perturbed by wave refraction over currents (*13*). A more exhaustive analysis of the full swell field, including shorter distances, could use a partitioning of the spectrum with watershed methods and cross-assignment of the partitions to the different storms (*40*).

From the masked spectrum, the swell height H_{ss} is defined as $4\sqrt{E_{mask}}$ where E_{mask} is twice the sum of the masked energy. The factor two corrects for the two-sided nature of the spectrum. The energy wavelength L_E is given by the square of the ratio of the masked energy weighted by $1/\sqrt{k}$ and E_{mask}. This is equivalent (for linear waves in the absence of currents) to the energy period T_E from the ratio of the -1st and 0th moments of the wave spectrum, namely $L_E = gT_E^2/(2\pi)$.

Propagation of analytical spectral shapes on the sphere: isotropic case

This is exactly the analysis done in (*19*), which we repeat here in a slightly different form. We use R_E the Earth radius and α is the spherical distance, so that a distance along a great circle is $d = \alpha R_E$. We consider observations at time t_o at a location of colatitude and longitude (λ_O, φ_O), and the measured spectrum is one two-dimensional map from a 5-dimensional spectral density field $E(\lambda, \varphi, t, f, \theta)$.

The total wave energy at point O is the sum over the wave spectrum, i.e.

$$E_O = \int_0^{2\pi} \int_0^{\infty} E(\lambda_O, \varphi_O, t_o, f, \theta') df d\theta' \quad (1)$$

We now express this observed energy as a function of the wave field at a previous storm time t_s, and we assume that, as schematized on Fig. S1, all the long period waves are contained within the shaded region which represents a storm.
Using the conservation of spectral densities (*17*), we get this sum

$$E_O = \int_0^{2\pi} \int_{f_1}^{f_2} E(\lambda_P, \varphi_P, t_s, f, \theta) df d\theta' \text{ with } f = g(t_o - t_s)/(4\pi\alpha' R_E) \quad (2)$$

A more elegant but possibly more obscure derivation is in Appendix C of (*19*).

We can now use different simplifying assumptions. The most simple case is that we assume that the wave spectrum within the shaded area is uniform and isotropic, with a value

$$E_S(f,\theta) = E_{S,iso}(f)/(2\pi) \quad (3)$$

Defining Δθ' the range of azimuth angles over which the storm is seen from O, we use the spherical law of cosines in the triangle OPS, with P on the edge of the storm (at the maximum azimuth θ' for a given distance α'), i.e. the colatitude is given by the storm radius r, $\lambda_P = r/R_E$,

$$cos(\Delta\theta'/2) = \left(cos(r/R_E) - cos\alpha \cdot cos\,\alpha'\right)/(sin\alpha \cdot sin\alpha') \quad (4)$$

and the observed energy is now a simple sum over the distances α'

$$E_O = \int_{f_1}^{f_2} E_{S,iso}(f)/(2\pi)\,\Delta\theta'\,df = \int_{\alpha_1}^{\alpha_2} E_{S,iso}(g(t_o - t_s)/(4\pi\alpha' R_E))\,\Delta\theta'\,(df/d\alpha')\,d\alpha'/(2\pi) \quad (5)$$

This integral can be evaluated numerically using any analytic expression for the source spectrum, which can be the JONSWAP spectrum (*5*) or the update proposed below with eqs. (8) and (9). This is done in the python notebook `dispersion_storm_isotropic.ipynb` (*30*).

In the limit where $|\alpha' - \alpha| \ll \alpha$ and $r \ll R_E$, which is appropriate far from the storm, we find that $\Delta\theta' \simeq \pi(r/R_E)/(2 \sin\alpha)$ when averaged from α_1 to α_2 and $df/d\alpha' \simeq f_\alpha/\alpha$ with
$f_\alpha = g(t_o - t_s)/(4\pi\alpha R_E)$,
and we get the asymptotic form

$$E_O(\alpha, SPP, r) = f_\alpha\, E_{S,iso}(f_\alpha)(r/R_E)^2/(2\,\alpha\, sin\,\alpha) \quad (6)$$

In the main text we have used this asymptotic form, which is independent of storm shape and internal structure, to fit a parametric swell height $H_{ss} = 4\sqrt{E_0(\alpha, SPP, r)}$ which gives an estimate of the storm peak period SPP and storm radius *r* from the SWOT and SWIM measurements. Note that we have not interpreted the radius *r* because a more complete model should take into account swell dissipation (*41*). We have verified with the numerical integration of eq. (5) that a realistic dissipation has no significant impact on the estimate of T_p .

A low-frequency update to usual spectral shapes

Measurements at sea by compiled by Lionel Moskowitz have led to an empirical spectral for fully developed seas that takes the form (*42*),

$$E_{PM}(f) = \alpha_P g^2 f^{-5} e^{-0.74\,(f_u/f)^4} \quad , \tag{7}$$

With α_P=0.0081/(2π)^4 the Phillips' constant. This form, known as the "Pierson-Moskowitz" spectrum was later updated by Hasselmann (*5*) to also represent relatively young waves for which ,

$$E_J(f) = \alpha_P g^2 f^{-5} e^{-1.25\,(f_p/f)^4} \gamma^{exp\left(-(f-f_p)^2/2\,\sigma^2 f_p^2\right)} \quad . \tag{8}$$

where the "peak enhancement factor" was found to be γ=3.3 for fetch-limited conditions, and the width of this peak enhancement region σ was set to σ=0.07 for f < fp and σ=0.09 for $f>f_p$, suggesting that the peak should be steeper on the low frequency side of the spectrum. In practice the JONSWAP form is often used with σ=0.07 on both sides of the peak, which we have done here.

We propose to keep the part of the spectrum for frequencies above peak (for $f>f_p$) and update the lower frequencies $f<f_p$ with,

$$E_J(f) = \alpha_P g^2 f_p^{-5} (f/f_p)^{n\,tanh(5(f_p-f)/f_p)} e^{-1.25} \gamma^{exp(-(f-f_p)^2/2\,\sigma^2 f_p^2)} \tag{9}$$

In practice we use *n=17*, and although the classical JONSWAP spectrum probably has γ=1.3 to 1.7 for the storm conditions considered here (*43*), it is not clear what should be the value of γ for phenomenal seas. Since our spectral shape reduces the total energy (Fig. S2.A), we have compensated this effect by using a constant γ=2 giving spectral shapes in Fig. S2.B. Alternatively γ might be fitted on the SWOT data, but it is sensitive to a range of frequencies where few data are available. Our estimates of the storm peak period are not very sensitive to the choice of γ, with Tp=19.2 for γ=1.3 and Tp=19.3 for γ=2 in the case of storm Bolaven.

Propagation combining different analytical spectra for different source regions

Numerical simulations of eq. (5) have been used to evaluate the impact of different effects on the fitted peak periods: dissipation, non-uniformity of the source region, error in the source position. Fig. (S4) illustrates the typical effect of a smaller area with larger wave heights and periods

surrounded by a wider region with lower wave heights and periods. The resulting distribution of swell heights has two maxima: fitting only the peak that is further from the storm allows to get a more accurate estimate of the longest periods (19.9 s instead of the input 20 s) and fitting a wider range of distances / wavelengths tends to reduce the fitted period (19.1 s in Fig. 23.C). These simulations have led us to use the data selection criteria defined below.

Data selection criteria and estimation of the Storm Peak Period (SPP): a 4-step algorithm

Our analysis is based on all the swell partitions observed along a single satellite track. It is based on the expected evolution of L_E and H_{ss} as a function of distance from the storm d.

Step 1: based on the model storm catalog (*28*) an a priori distance to storm d and time from storm t_o-t_s is defined for each swell observation. The analytical model is fitted to these observations based on the measured L_E , which provides a refined storm time and along-track position that is used in the next steps, with an updated distance to storm d. The fit uses an unweighted least square and is implemented in the notebook L3_fit_one_track_LandH.ipynb (*29*).

Step 2: We select the largest set of measurements of H_{ss} that are contiguous along the track starting from [500 , 1050] as a range of accepted values of L_E. Note that these wavelengths correspond to periods T_E of 18 and 26 s. We note that a narrower range could be defined for different tracks but was not retained here for automatic processing. This range is extended towards higher and lower wavelengths provided that L_E is within 3% of the expected value (based on the analytical fit) for low values of L_E. SWOT can resolve swells as short as 500/√2 = 340 m when they propagate at 45° from the satellite track, but because L_E is an average, having L_E=500 m means that some of the energy is at wavelengths shorter than 500 m and is likely to be missed for some propagation directions. These shorter components can also be aliased and either underestimated or attributed to a wrong direction (*13*). For the large wavelength we use a more relaxed threshold of 7.5% of the expected value, and only keep the data for which H_{ss} decreases as a function of distance and H_{ss} must be larger than 10cm . A first fit of SPP and r is performed using this set of swell height and the asymptotic model in eq. (6).

Step 3: If the wavelength corresponding to SPP, i.e. $L_{SPP} = g\ SPP^2 / 2\pi$, is larger than lowest L_E used in the H_{ss} fit of step 2, then we restrict the data range to only have L_E higher than L_{SPP} and perform a second fit of Hss using eq. (6) which provides our final estimate of SPP, as listed in tables S2 and S1. The automatic processing of all satellite tracks mentioned in Table S1 (and more) is performed by the notebook L3_fit_all_tracks_LandH.ipynb

Step 4: Quality control

The quality of the fit is summarized in a Mean Absolute Percentage Error (MAPE) between L_E observed ($L_{E,obs}$) and the fitted value, and similarly for the swell heights (see Table S1). Also, if there is no peak in the fitted swell heights after Step 2 then the SPP estimate is “not successful” and the fitted value of SPP is considered to be an upper bound of the value that could be obtained if shorter swells were resolved by SWOT.

The automatic processing of all satellite tracks mentioned in Table S1 (and more) is performed by the notebook L3_fit_all_tracks_LandH.ipynb All data were processed with the same settings

except for the following adjustment: for storms Kirk and Solveig the thresholds that define the partition in the spectrum were adjusted to avoid combining swells from 2 different storms: we used a relative tolerance of 20% (instead of 30%) on the spatial frequencies included in the swell partition.

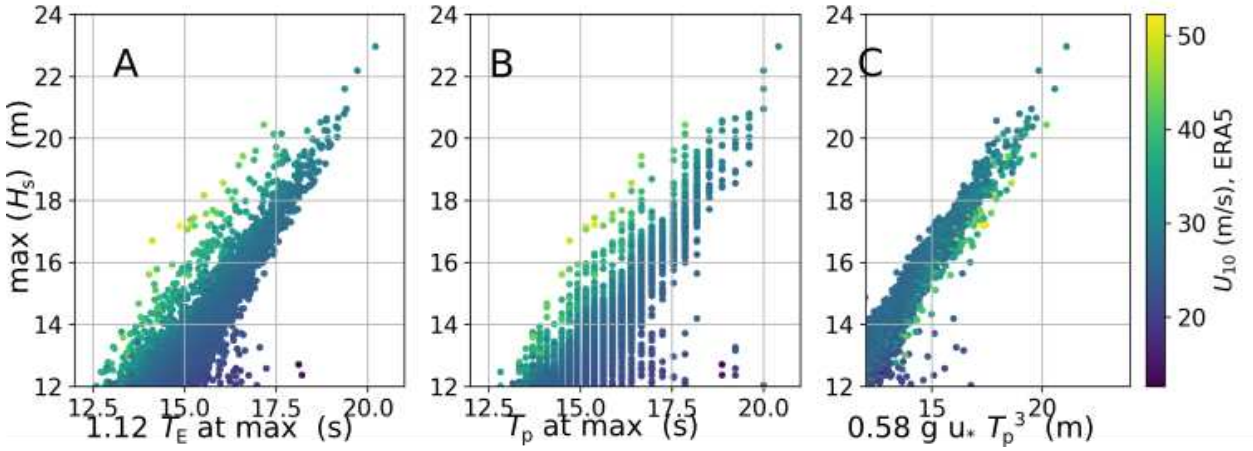

Fig. S1.
Joint distribution of modeled wave height Hs and peak period at the storm peaks, with colors showing the wind speed from ERA5 (A) Tp is replaced by 1.12 T_E to avoid discretization effects in the model. (B) uses Tp and (C) Tp is converted to wave height using Toba's Law with a slightly adjusted parameter: 0.58 instead of Toba's 0.62 (*2*). Here the friction velocity u_* is obtained from the wind speed in ERA5 reanalysis (*21*) at the location of the modeled Hs maximum (*9*) and a constant drag coefficient 0.0025.

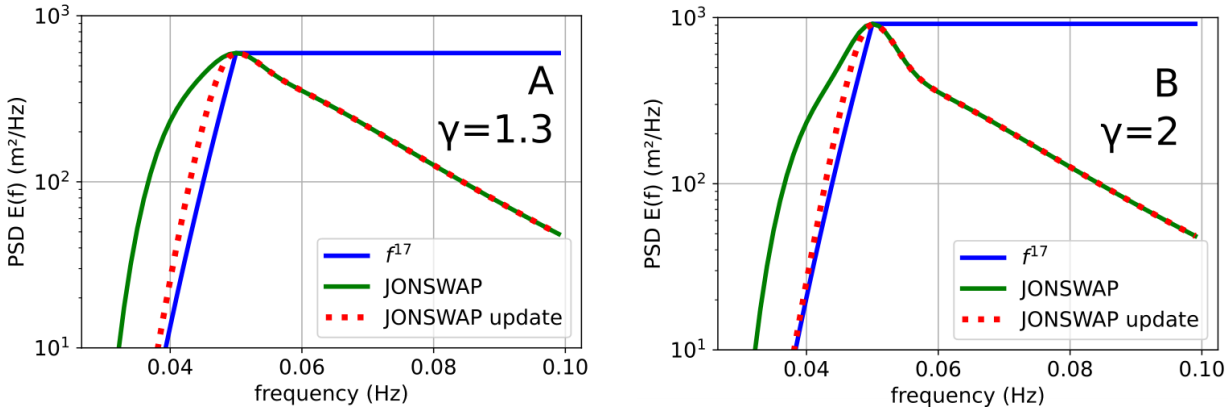

Fig. S2.

Empirical "JONSWAP" form for the wave spectrum (5) and our proposed updated spectral shape given by eq. (3). This is shown for two values of the shape parameter γ that gives some peak enhancement.

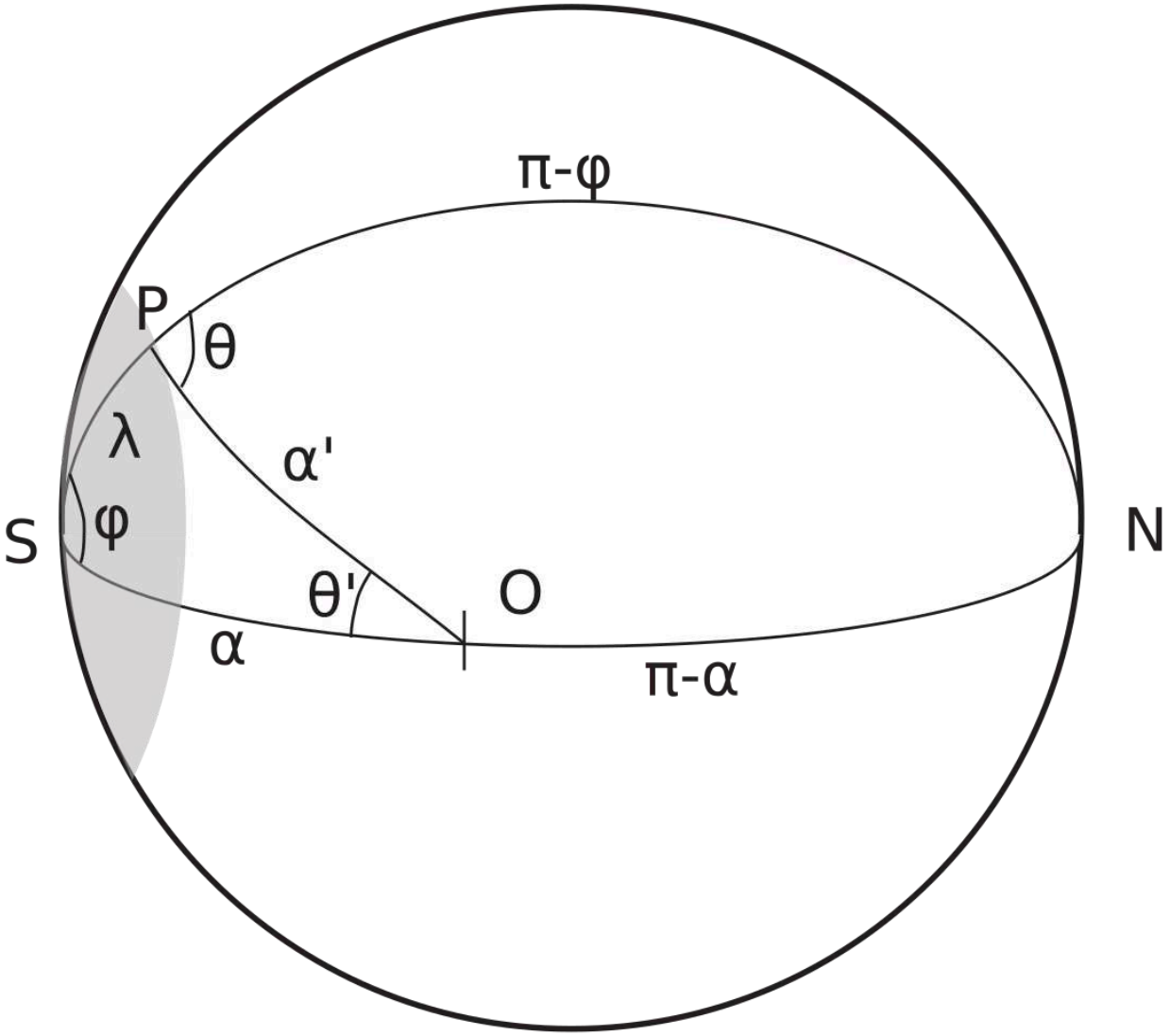

Fig. S3.

Schematic of wave propagation on the sphere. The analytic propagation model is based on a wave spectrum within the shaded area that is constant and isotropic at time t_s, with a value $E_S(f,\theta)$. These waves propagate and are observed at time t_o at point O.

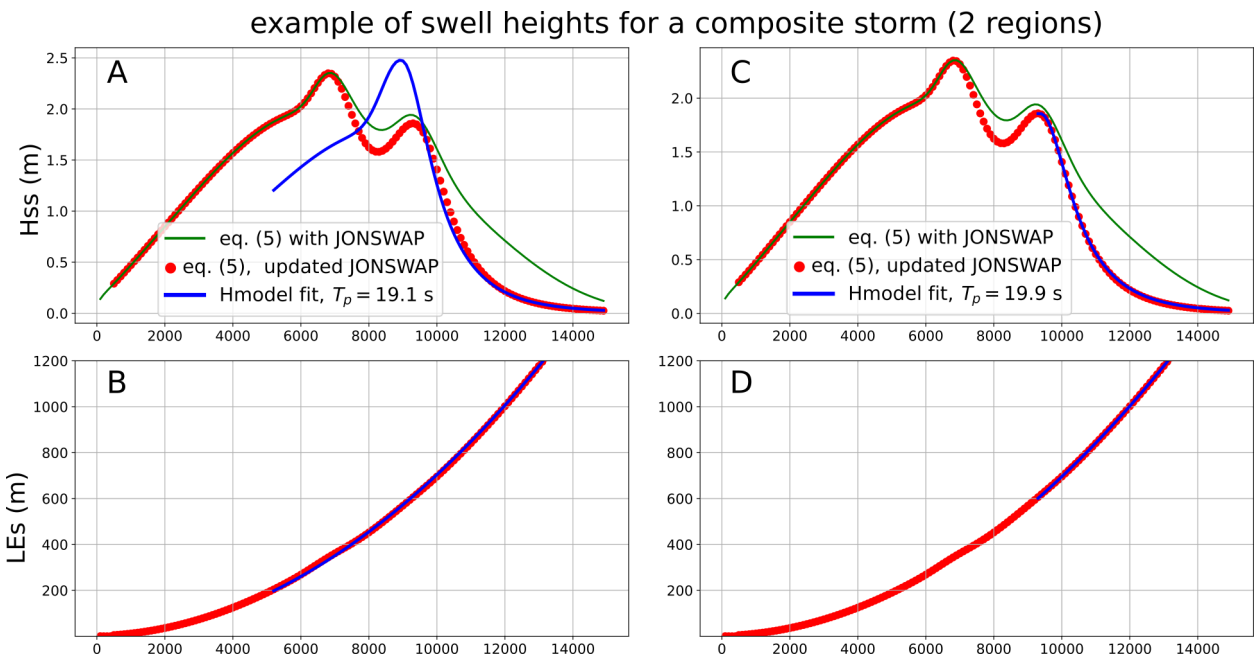

Fig. S4.

Example of simulated swell height and wavelength using the analytic propagation model, for a composite storm that includes two regions: region 1 with 300 km radius, centered at x=0, Tp=20s, region 2 with 600 km radius, centered at x=-300 km, Tp=15.4s. Note that the 2nd region covers the 1st region: when we combine the two, we remove energy from the second region in the intersection. The simulated data is fitted in the same way as the SWOT data in Fig. 2, using either a wide range of wavelengths in (A,B) or a restricted range in (C,D).

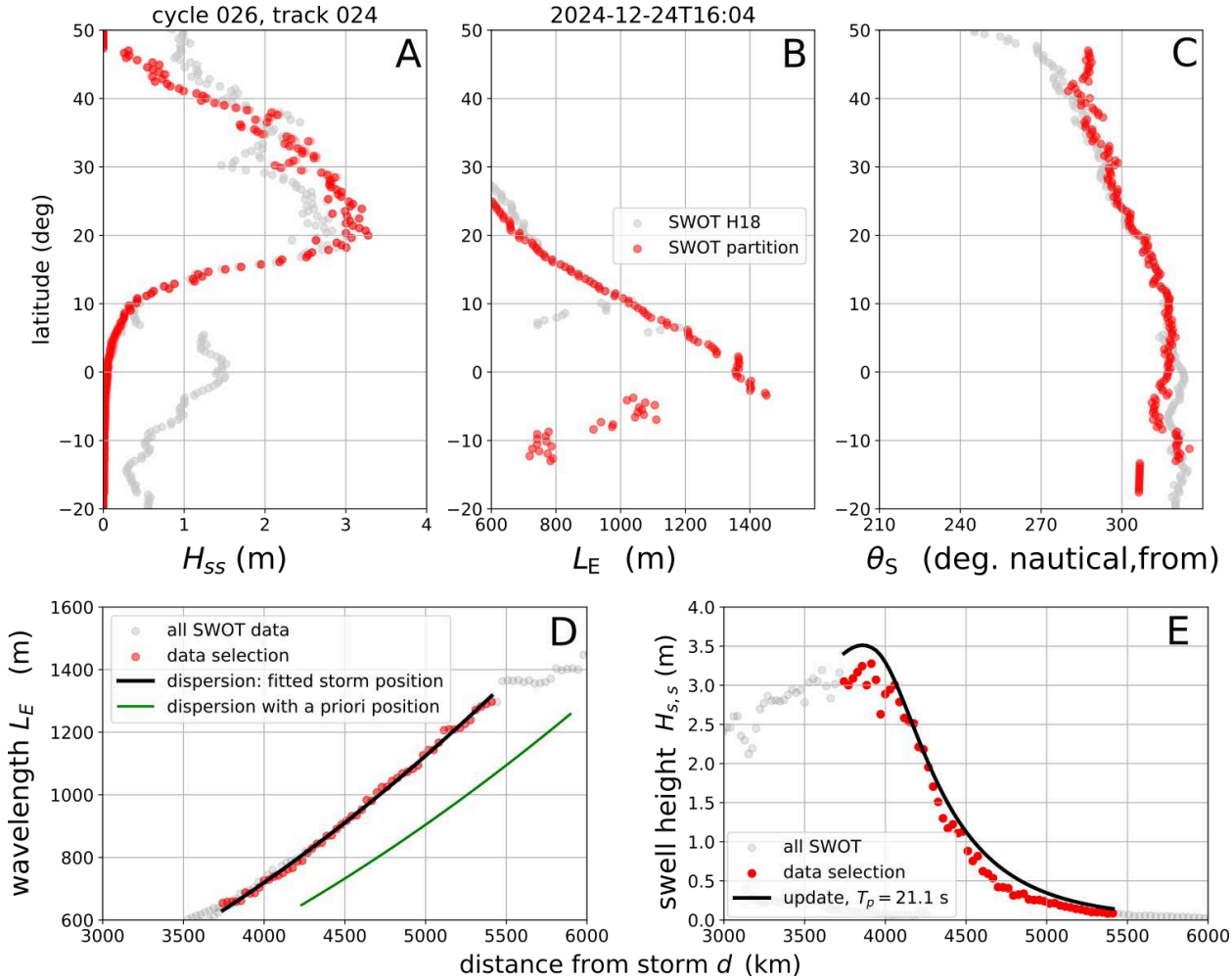

Fig. S5. Swells from storm Edie as captured by SWOT on cycle 026 track 024 on 24 December. A-C show partition heights, wavelengths and direction as a function of latitude (the grey dots are the H18 and L18 as computed in the CNES L3 WIND-WAVE product). (D) and (E) are similar to Figure 2.A and 2.B. Here the data selection was forced to use L_E in the range [650 ,1300]. Note that the discontinuous behaviour of L_E for L_E > 1200 m is caused by our use of a coarse wave spectrum.

Table S1.

This table provides the background information for SPP estimates from SWOT shown in Fig. 3C. Storms are uniquely identified by their ranking in the Ardhuin-De Carlo storm catalog (*28*), or for simplicity, by a name (e.g. ADC-0005 is called "Eddie"). SWOT data are defined by their cycle number, track number, and the side sub-swath which can be either left (L) or right (R). Before July 2023, for cycles above 300, SWOT is on a 1-day repeat orbit and the track positions are the same from one day to the next (see movie S1). After July 2023, the SWOT orbit repeats over each cycle that has a 21 day duration. From one day to the next, the track n+28 is shifted west by about 3° in longitude compared to track n of the previous day (e.g. red and blue tracks on Fig. 1.B). See movie S1 for all track positions. The selection criteria that define $L_{E,min}$ and $L_{E,max}$ are described above. Values reported in the table are a selection based on: SPP < 25 s, mean(Hss) < 5m , $L_{E,max}$ > 700m, a Mean Absolute Percentage Error (MAPE) for the fitted H_{ss} less than 0.3, a MAPE for the fitted L_E less than 0.3, and a number of fitted values larger than 20. After this first selection, for any given storm we discarded the tracks with the largest MAPE for H_{ss} and we excluded tracks for which the best fit distribution of L_E is shifted by more than one day from the a priori storm peak. The discarded tracks are highlighted in red, and the number that caused this is in bold. For each storm a median and standard deviation of the Storm Peak Period is in the header.

SWOT cycle, track, side	$L_{E,min}$ (m)	$L_{E,max}$ (m)	SPP (s)	θ_S (deg,from)	time shift (days)	MAPE L_E fit	MAPE H_{ss} fit
Eddie* (ADC-0005): t_s=2024-12-21T15, lon_s=161W, lat_s=39°N, wind=28.9 m/s wave dir=273° Hs model (MMWH) = 20.8 m, **SPP = 19.9 ± 0.5 s**							
026 052 L	609	1263	20.1	306 ± 5	-0.387	0.007	0.102
026 078 L	712	1026	19.2	283 ± 5	-0.303	0.009	0.128
026 080 L	566	1041	19.7	316 ± 3	-0.06	0.007	0.192
026 106 L	585	1047	20.5	297 ± 6	-0.304	0.006	0.084
026 108 L	603	1032	20.2	325 ± 3	0.03	0.007	0.108
026 134 L	605	1158	20.3	312 ± 8	0.121	0.006	0.117
026 136 L	559	1052	19.2	332 ± 3	0.482	0.01	0.103
026 190 L	573	955	19.5	329 ± 7	-0.838	0.018	0.154
026 024 R	646	1221	20.9	289 ± 7	-0.411	0.020	**0.218**
026 052 R	613	1045	20.1	305 ± 4	-0.346	0.013	0.058
026 078 R	702	1208	21.3	287 ± 6	-0.255	0.009	**0.285**
026 106 R	584	1174	20.5	299 ± 8	-0.147	0.007	0.084
026 108 R	603	1102	20.1	326 ± 3	-0.025	0.006	0.099
026 134 R	606	1043	20.3	310 ± 7	0.09	0.005	0.084
026 136 R	576	1022	19.4	332 ± 3	0.505	0.009	0.115
026 190 R	563	961	19.1	329 ± 7	-0.939	0.017	0.109
Bolaven (ADC-0013): t_s=2023-10-16T01, lon_s=174W, lat_s=42°N, wind=30.0 m/s wave dir=264° Hs model (MMWH) = 20.3 m, **SPP =19.3 ± 0.5 s**							
005 218 L	627	991	19.7	278 ± 5	**1.407**	0.011	0.144

005 246 L	605	1102	19.7	292 ± 6	0.553	0.017	0.114
005 274 L	574	1032	19.4	303 ± 6	0.375	0.009	0.111
005 300 L	630	1033	19.7	286 ± 10	0.558	0.009	0.071
005 328 L	583	1043	19.7	301 ± 12	0.136	0.009	0.055
005 356 L	516	828	18.4	309 ± 9	0.267	0.005	0.102
005 218 R	618	995	19.9	279 ± 6	**1.313**	0.01	0.158
005 246 R	599	1092	19.7	293 ± 6	0.589	0.017	0.112
005 274 R	574	1044	19.4	304 ± 6	0.336	0.008	0.116
005 300 R	625	1031	19.7	290 ± 8	0.508	0.008	0.067
005 328 R	588	1047	19.6	301 ± 11	0.141	0.009	0.052
005 356 R	525	843	18.4	310 ± 8	0.081	0.006	0.116
Kirk (ADC-0017): t_s=2024-10-06T08, lon_s=49°W, lat_s=33°N, wind=39.4 m/s wave dir=175° Hs model (MMWH) = 20.1 m, **SPP < 18 s**							
022 199 L	511.0	877.0	<9.1	205±3	1.022	0.052	0.431
022 199 R	516.0	858.0	<7.8	205±2	0.174	0.012	0.39
022 253 L	504.0	624.0	<14.6	204±2	0.97	0.015	0.196
022 253 R	512.0	657.0	<15.4	205±3	0.903	0.011	0.165
Bertrand* (ADC-0056): t_s=2023-09-15T21, lon_s=16°E, lat_s=47°S, wind=30.6 m/s wave dir=244° Hs model (MMWH) = 19.2 m, **SPP = 19.3 ± 0.4 s**							
003 551 L	579	1015	19,6	258 ± 6	0.068	0.017	0.188
003 579 L	551	826	19.1	249 ± 3	-0.126	0.018	**0.233**
003 551 R	594	1062	19.6	259 ± 6	-0.008	0.009	0.161
003 579 R	553	787	18.9	250 ± 3	0.048	0.013	0.138
Romain* (ADC-0092): t_s=2023-11-22T01, lon_s=179°W, lat_s=45°N, wind=29.2 m/s wave dir=267° Hs model (MMWH) = 18.5 m, **SPP = 19.0 ± 0.3 s**							
007 080 L	572	991	19.6	284 ± 5	-0.011	0.012	**0.204**
007 136 L	561	971	19.1	308 ± 4	-0.134	0.005	**0.210**
007 162 L	549	1047	19.1	291 ± 8	0.586	0.01	0.135
007 164 L	542	915	18.9	316 ± 4	0.067	0.007	0.191
007 190 L	561	989	19.4	302 ± 8	0.397	0.007	0.065
007 192 L	545	929	15.9	324 ± 4	0.483	0.01	**0.211**
007 218 L	552	869	18.7	311 ± 8	-0.161	0.005	0.071
007 080 R	567	992	19.5	285 ± 5	-0.055	0.013	**0.211**
007 136 R	555	969	18.8	308 ± 4	-0.106	0.007	0.192
007 162 R	543	1047	19.1	292 ± 8	0.634	0.01	0.134
007 164 R	538	934	18.8	317 ± 4	0.016	0.011	0.160
007 190 R	564	991	19.5	303 ± 8	0.295	0.007	0.077
007 218 R	545	859	18.6	312 ± 7	-0.05	0.007	0.070

SWOT cycle. track. side	$L_{E.min}$ (m)	$L_{E.max}$ (m)	SPP (s)	θ_S (deg.from)	time shift (days)	MAPE L_E fit	MAPE H_{ss} fit
Manoa* (ADC-0192): t_s=2024-11-02T05. lon_s=156°W. lat_s=52°N. wind=27.4 m/s wave dir=252° Hs model (MMWH) = 17.7 m. **SPP = 18.4 ± 0.1 s**							
023 358 L	540	1126	18.4	297 ± 5	0.202	0.029	0.213
023 358 R	529	1109	18.3	298 ± 4	0.136	0.027	0.243
Hina* (ADC-0218): t_s=2024-01-03T00. lon_s=167°W. lat_s=49°N. wind=29.1 m/s wave dir=224° Hs model (MMWH) = 17.5 m. **SPP = 18.6 ± 0.2 s**							
009 162 L	521	945	18.8	299 ± 4	0.186	0.010	0.192
009 190 L	519	926	18.5	308 ± 5	0.217	0.010	0.155
009 218 L	527	908	18.6	316 ± 5	0.406	0.007	0.08
009 162 R	525	967	19.1	300 ± 4	0.163	0.009	0.130
009 190 R	523	942	18.3	309 ± 5	0.18	0.009	0.123
009 218 R	525	888	18.6	317 ± 5	0.445	0.007	0.076
Vehiatua* (ADC-0471): t_s=2024-02-17T09. lon_s=173°E. lat_s=50°N. wind=26.5 m/s wave dir=234° Hs model (MMWH) = 16.4 m. **SPP = 18.1**							
011 164 L	505	1021	18.1	277 ± 5	0.023	0.021	0.299
011 192 L	501	959	<17.3	290 ± 4	0.119	0.018	**0.262**
011 220 L	502	877	<17.5	300 ± 3	0.323	0.016	**0.271**
011 220 R	502	864	<17.6	301 ± 3	0.367	0.017	**0.273**
Moea* (ADC-0489): t_s=2023-10-12T14. lon_s=176°W. lat_s=50°N. wind=28.0 m/s wave dir=298° Hs model (MMWH) = 16.4 m. **SPP < 18 s**							
005 162 L	517	931	<8.5	283 ± 4	0.596	0.008	**0.247**
005 190 L	505	817	<15.6	291 ± 3	0.477	0.008	0.162
005 218 L	499	768	<10.6	299 ± 3	0.58	0.007	0.15
005 246 L	498	735	<10.2	308 ± 3	**1.146**	0.005	0.169
005 300 L	503	702	<15.3	305 ± 6	**1.309**	0.009	0.084
005 162 R	503	924	<9.6	283 ± 4	0.596	0.009	**0.222**
005 190 R	507	783	<15.5	291 ± 3	0.555	0.006	0.148
005 218 R	498	771	<9.9	300 ± 3	0.398	0.006	0.166
005 246 R	501	724	<14.7	308 ± 3	**1.363**	0.006	0.192
005 300 R	505	703	<15.2	306 ± 6	**1.348**	0.008	0.087
Matahina* (ADC-0496): t_s=2023-11-30T07. lon_s=174°E. lat_s=51°N. wind=27.5 m/s wave dir=237° Hs model (MMWH) = 16.4 m. **SPP = 18.5±0.2 s**							
007 276 L	501	1016	18.1	290 ± 3	-0.028	0.010	0.118
007 304 L	511	942	18.5	303 ± 2	-0.470	0.011	0.171
007 304 R	520	934	18.6	304 ± 2	-0.519	0.011	**0153**
Herenui* (ADC-0555): t_s=2023-12-04T06. lon_s=154°W. lat_s=44°N. wind=25.8 m/s wave dir=254° Hs model (MMWH) = 16.2 m. **SPP = 18.4 ±0.1 s**							
007 440 L	515	926	18.6	300 ± 4	0.569	0.009	0.105
007 440 R	504	930	18.3	300 ± 4	0.551	0.011	0.105
Manaarii* (ADC-0563): t_s=2023-12-22T03, lon_s=177°W, lat_s=46°N, wind=27.3 m/s wave dir=263° Hs model (MMWH) = 16.2 m, **SPP = 19.2 ±0.1 s**							

008 412 L	555	954	19.2	285 ± 5	-0.185	0.006	0.074
008 440 L	547	1003	19.2	298 ± 7	0.027	0.005	0.125
008 468 L	563	893	19.2	308 ± 7	0.285	0.009	0.186
008 412 R	545	956	19.1	286 ± 5	-0.146	0.006	0.059
008 440 R	543	968	19.1	298 ± 7	0.073	0.005	0.113
008 468 R	500	887	19.4	309 ± 7	0.186	0.007	**0.181**
Solveig* (ADC-0656): t_s=2024-12-15T11. lon_s=177°E, lat_s=49°N, wind=26.8 m/s wave dir=224° Hs model (MMWH) = 16.0 m							
026 022 L	502	791	17.8	283 ± 7	**2.092**	0.007	0.154
026 050 L	614	777	15.7	302 ± 6	**2.127**	0.008	0.152
026 022 R	499	771	17.8	282 ± 6	**1.941**	0.006	0.138
026 050 R	501	765	15.6	296 ± 9	**2.44**	0.007	0.166

Movie S1.

Visualization of modeled wave heights H_{18} (i.e. corresponding to the range of wavelengths L > 500 m typically resolved in SWOT Low Resolution data) and SWOT satellite tracks. The threshold at 5 cm is expected to be close to the threshold for swell detection by SWOT in most conditions. The model used here is described in (*9*).